Electromagnetic and Mechanical Topology Optimization for SynRM Rotors Considering High Dimensional Constraints Based on SIMP Method

Yu Li, Bo Ma, Jing Zheng, Jianguo Zhu, *Senior Member*, and Gang Lei, *Member*

***Abstract*—The knowledge-based parametric design process of the rotor topology of the synchronous reluctance motor (SynRM) requires a tedious parameter definition, selection, and searching process until an optimal design can be obtained. This research proposes a topology optimization approach based on solid isotropic material with penalization method for the SynRM rotor topology design. The aim is to pursue a more intelligent and automatic design process. Specifically, the proposed method aims to generate the SynRM rotor design of high output torque profile. Meanwhile, the mechanical constraints including structural compliance and stress etc. are also considered for promising the structural reliability of the rotor. Considering the high dimensional constraints caused by the multi-physics performances, the augmented Lagrangian method based optimization framework is developed to solve the minimization problem in a compact scheme. To prove the effectiveness of the developed method, simulations and analysis on the topology optimization of SynRMs are performed in this research. Prototyping and experiment are also conducted for verifying the performance of the optimized structure.**

***Index Terms*—Topology optimization, synchronous reluctance motor, multi-physics, solid isotropic material with penalization, augment Lagrangian method.**

I. Introduction

Synchronous reluctance machines (SynRMs) possess the merits of cost-effectiveness without utilizing permanent magnets, proper efficiency and simple structure, etc., and thus they have been widely employed in the drive and power generation field [1-4]. Since the rotor structure of the SynRM plays a decisive role in the drive performance, it is carefully designed to achieve high torque density, lightweight, and high mechanical stiffness and strength. However, the traditional shape design is experience-based and generally requires a tedious parametric optimization process until an optimal design can be achieved. This procedure generally requires a massive effort on the initial structure proposal. Furthermore, the computational burden of the parameter optimization process depends on the complexity of the initial shape proposed by the designers. The more complicated the initial design is, the more time-consuming the optimization can be [5-7].

An intelligent and automatic SynRM rotor design process always pursues high torque density and mechanical reliability. The topology optimization is the design optimization to automatically solve the problem of placing material in the design domain for the best performances [8,9]. Unlike the traditional parametric size or shape optimization that started with a well-designed initial geometry, the topology optimization aims to decrease the expertise dependence on the initial structure design and realize the conceptual design and quantitative optimization in the same automatic process. Due to the advances in the methods, topology optimization has been spreading from the mechanical field to structural design optimization in other disciplines, including the design optimization of electrical machines [10-12].

In the rotor design process of the SynRMs, the designers care about several primary aims, including the output torque/power density. To achieve this goal, the SynRM rotor design by topology optimization is to determine where the vacuum (air barrier) part and electrical steel are in an exact domain. For example, specific topology optimization methods such as the level set method [13,14], Gabor Filter method [15], deep learning-based method [16], and solid isotropic material with penalization (SIMP) method [17-20], normalized Gaussian network method [21], have been investigated to improve the torque profiles of SynRMs.

Meanwhile, the mechanical stiffness and strength of the rotor should also be considered in the optimization process for promising mechanical reliability in the operation range. Some pioneering works on the SynRM rotor topology optimization have been contributed recently. For example, electromagnetic shape design and structural topology optimization are investigated in [17,18] for the high mechanical performance rotor design. However, the electromagnetic output and mechanical performances are optimized in a sequential process in this work. The steel ribs are generated by the structural topology optimization in the air domain, so the optimized torque obtained in the first step cannot be promised since the existence of the ribs will cause flux leakage that decreases the

electromagnetic performance.

Considering the electromagnetic and mechanical performance enhancement concurrently, the research in [19] presents the topology optimization for the SynRM rotor electromagnetic torque and structrual compliance for the structural safety enhancement with multiple ribs. Moreover, to consider the mechanical performance more comprehensively, the mechanical stress concentration should also be avoided at the same time while pursuing the high strength and torque density. However, a large number of constraints would be involved since the number of stress constraints equals the element or node number in the design domain. To overcome this difficulty, the clustering techniques such as the p-norm method has been applied for aggregating the stress constraints into one constraint, and then the number of constraints is decreased [22]. On the other hand, difficulty in finding a suitable p-value has been pointed out, i.e., the high value increases the nonlinearity while the low value dilutes the effectiveness of the stress constraints [9]. Moreover, the aforementioned research considering the electromagnetic and mechanical features of the SynRM is also conducted in multiple stages, which may affect the convergence to the optimal solution. In order to address the design requirements for high electromagnetic output torque, lightweight, and mechanical stiffness and strength, this research developed a topology optimization approach for the rotor design of SynRMs. Compared with the former study, the contribution of the paper mainly includes the following aspects:

(1) A multi-physics topology optimization formulation is built for the SynRM rotor with the SIMP interpolation scheme for multiple material properties to consider electromagnetic and mechanical performances in a compacted scheme.

(2) An equivalent augmented Lagrangian (AL) function is established to simultaneously incorporate the high-dimensional multi-constraints related to electromagnetic and mechanical performances. To the authors' best knowledge, the establishment of the framework is developed for the first time in the field of SynRM design. Moreover, the sensitivities derivation of the objective and constraints to the topological design variables are illustrated clearly.

(3) The effectiveness of the developed approach is verified on a SynRM design sample. The SynRM prototype with the optimized rotor structure is manufactured, and the performance of the SynRM is validated by experiments.

The remaining sections of the paper are arranged as follows. Section II presents the introduction of the SIMP method and the detailed interpolation scheme of the relevant material properties. Section III demonstrates the system functions of the electromagnetic and structural finite element analysis (FEA) for the performance calculation of the SynRM and the topology optimization modeling. Section IV presents the AL function establishment process, followed by the sensitivity analysis of the AL model to the design variables and optimization framework construction. Section V offers the topology optimization of the example SynRM rotor with the established optimization method, and Section VI validates the performance of the SynRM with the obtained rotor structure. Finally, Section VII draws the conclusions.

II. SIMP Method and Material Interpolation Scheme

A. Topology Optimization Introduction and Basic Steps

In the research field of structural optimization, the optimization methods are generally divided into three categories: size optimization, shape optimization, and topology optimization. The schematic diagram of the optimization methods is illustrated in Fig.1. The size optimization can only be used to optimize dimensions of the existing geometries and the shape optimization improve the performance of structures by optimizing the boundary features. Both above methods rely on the designers' experience in providing the well-constructed initial design and the optimization freedom is limited.

Combing the FEA method which divides the design domain into finite elements, the topology optimization method provides a numerical iterative process that can distribute materials within the design domain for obtaining optimal design automatically. Among the three kinds of structural optimization methods, topology optimization is regarded as of the highest level, since it can realize the conceptually and quantitively optimal design in the design domain.

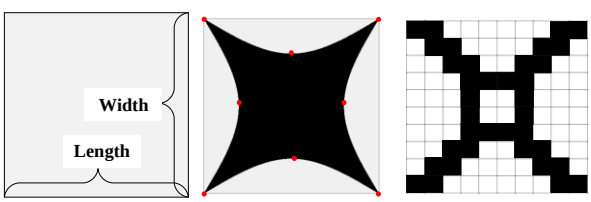

Fig. 1. Schematic diagram of difference among the optimization methods including (a) Sizing, (b) shape, and (c) topology.

Since topology optimization aims to arrange the material of each element, the design variables number equals to the number of elements or nodes in the design domain. There are generally hundreds or thousands of elements in the rotor design domain of the 2D FEA model of SynRM, which leads to the high dimensional discrete optimization problem of high solving difficulty. Utilizing the SIMP method, the high dimensional discrete optimization problem is transferred into a continuous one with low computational difficulty. To take advantage of the SIMP method for the topology optimization of SynRM, the basic setting steps includes:(1) material interpolation according to SIMP method; (2) design domain selection and optimization modeling; (3) FEA formulation and computation. The detailed establishment process of the above matters are introduced below.

B. Material interpolation of the SIMP Method

There are two materials, i.e., electrical steel and air, in the SynRM rotor design domain. as demonstrated in Fig. 2, the topology optimization method aims to solve the material placing problem in each element. However, the number of design variables equals the element amount in the design domain. The optimized design can hardly be obtained for this

large-scale mathematical programming problem if the two materials are represented and arranged discretely.

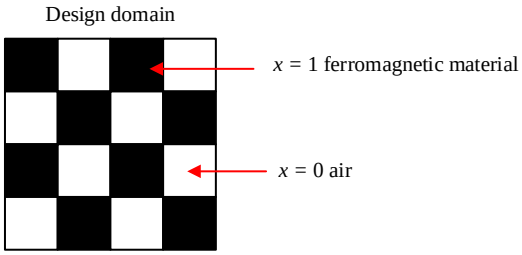

Fig. 2. Using discrete 0 and 1 to represent the material distribution of elements in the design domain.

By adopting the SIMP method, the discrete problem can be transferred into a continuous one by the material property interpolation, in which the design variable x is defined as a continuous variable varying in the range of [0,1]. As illustrated in Fig. 3, the air and electrical steel can be represented by $x=0$ and $x=1$, while $0<x<1$ means a virtual material with property between steel and air. Then the problem of finding the element material property can be solved by high-efficiency continuous gradient-based minimizing algorithms.

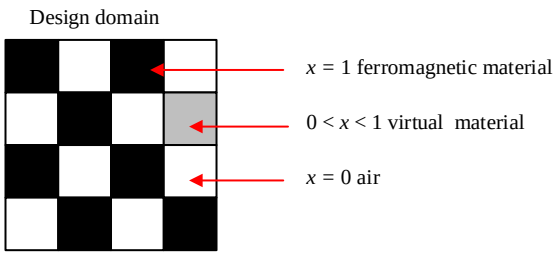

Fig. 3. Using continuous design variables in [0,1] to represent the material distribution of elements in the design domain.

Furthermore, when solving the high dimensional optimization, the numerical unstable problem can be encountered. The large-scale gray design with virtual intermediate material property or the checkboard result can be generated, which leads to a failed design. To mitigate the above issues, the three-field material interpolation scheme which takes advantage of the filtering and projection techniques is adopted in this research [9, 23]. The Helmholtz filtering and threshold projection are performed by adopting the three-field material interpolation to alleviate the localized features and promote smooth designs before the physical performance interpolation.

Since the electromagnetic and mechanical performance are mainly considered in this research, the material properties including permeability (or magnetic reluctivity), Young's modulus, and mass are generally used to distinguish electrical steel and air. The specific interpolation steps are introduced below. Firstly, the Helmholtz filtering of the design variable vectors is performed by

$$\boldsymbol{y} = \boldsymbol{\gamma x} \tag{1}$$

where $\boldsymbol{x}$ is the vector of the design variables, and $\boldsymbol{\gamma}$ is the filter matrix, in which the components are computed as

$$\gamma_{lk} = \frac{w_{lk}}{\sum_{j=1}^{N_e} w_{lk}} \tag{2}$$

$$w_{lk} = \max\left(0, 1 - \frac{\left\|\boldsymbol{z}_l - \boldsymbol{z}_k\right\|_2}{R}\right)^q, \tag{3}$$

where R is the radius of the filter, q the filter exponent, $\left\|\boldsymbol{z}_l - \boldsymbol{z}_k\right\|_2$ the distance between the centroids of elements with the subscripts l and k, N_e the number of elements in the design domain.

Then, the projection is performed in the following step for the smooth design

$$f_p(\boldsymbol{y}) = \frac{\tanh(\beta\eta) + \tanh(\beta(\boldsymbol{y} - \eta))}{\tanh(\beta\eta) + \tanh(\beta(1 - \eta))} \tag{4}$$

where β is the steepness of the projection and η the threshold value. After the filtering and projection of the design variable, the material property interpolation is performed.

The shape optimization of the SynRM rotor is the ferromagnetic material layout in the design space. For the electromagnetic performance analysis, magnetic reluctivity is selected as the distinction between the electrical steel and air in the static electromagnetic field computation. The material distribution in the design domain is defined by interpolating the reluctivity by

$$\boldsymbol{\nu} = \nu_{fe} f_p(\boldsymbol{y})^p + \nu_{air}\left(1 - f_p(\boldsymbol{y})^p\right) \tag{5}$$

where ν_{fe} and ν_{air} are the reluctivities of electrical steel and air, respectively, and p the penalization factor. Similarly, Young's modulus is selected to distinguish the steel and air in the structural field analysis. The adopted Young's modulus interpolation is expressed as

$$\boldsymbol{E} = E_{fe} f_p(\boldsymbol{y})^p \tag{6}$$

where E_{fe} is Young's modulus of electrical steel. The weight interpolation for each element in the rotor design domain is also required to consider the mechanical load of a rotating object. Since the triangular element for FEA of SynRM is inhomogeneous, the weight interpolation of the element volume can be expressed as

$$\boldsymbol{m} = \boldsymbol{m}_{fe} \odot f_p(\boldsymbol{y}) \tag{7}$$

where $\boldsymbol{m}_{fe}$ is the physical mass vector of the elements supposing the material of the element is electrical steel, $\odot$ the Hadamard product. By the interpolation, the properties $\boldsymbol{\nu}$, $\boldsymbol{E}$ and $\boldsymbol{m}$ of the virtual material for each element in the design domain are determined.

C. Design Domain Setting and Optimization Modelling of the SynRM Rotor

To reduce the computational cost, the partial model with periodic boundary is widely utilized for the FEA. Taking the 1/4 model of the 4 pole motor as an example, to promise the symmetry of the rotor structure, half of the rotor domain is set as the design domain. As shown in Fig. 4, the mesh in the design domain is generated at first, and then the mesh is mirrored to

the other half domain of the rotor. The design variables are only defined for the elements in the design domain for determining the material properties. The obtained material properties of the mirrored elements are set the same as the relevant ones in the design domain. Then the design number of the design variables is effectively decreased by the above setting method. On the other hand, the symmetrical structure obtained by the optimization can promise the boundary conditions to be met and the same torque performance when the motor rotates in a different direction.

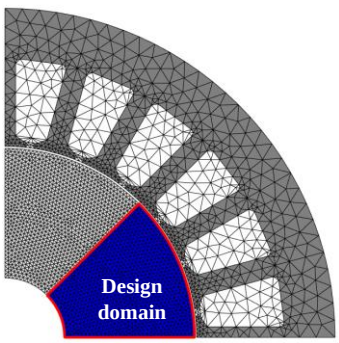

Fig. 4. Design domain of the SynRM.

The combined model considering both electromagnetic and mechanical performances to ensure output torque performance, and mechanical stiffness (structural compliance) and strength can be defined as

$$\min: f = -\frac{1}{n}\sum_{i=1}^{n} T_i$$
$$\text{s.t.}\begin{cases} g_j(x) = \sigma_j^v - \sigma_{\lim} \le 0,\ j = 1,\ldots,N_e \\ g_{N_e+1}(\boldsymbol{x}) = \boldsymbol{m}^T\boldsymbol{I} - a_r \boldsymbol{m}_{\boldsymbol{fe}}{}^T \boldsymbol{I} \le 0, \\ g_{N_e+2}(\boldsymbol{x}) = C - C_0 \le 0, \\ g_{N_e+3}(\boldsymbol{x},\boldsymbol{A}) = T_{vr} - T_{vr0} \le 0 \end{cases} \tag{8}$$

where n is the rotor position number for torque computing, T_i is the torque at the i_{th} rotor position, σ_j^v the Von Mises stress of the element in the design domain, the subtitle j means the element number, $\sigma_{\lim}$ the permissible stress of the material, $\boldsymbol{I}$ the vector of ones, a_r the percentage of the mass, C the structural compliance of the rotor structure, C_0 the given reference structural compliance, and T_{vr0} the given reference torque ripple. T_{vr} the variance of the torque in the sampled rotational points, which is expressed as

$$T_{vr} = \frac{\sum (T_i - T_{av})^2}{n} \tag{9}$$

where T_{av} is the average torque.

For the fast driving of the solution toward the state of low stress than the limited value, the polynomial vanishing constraint technique is applied here, and the optimization model is formulated as

$$\min: f = -\frac{1}{n}\sum_{i=1}^{n} T_i$$
$$\text{s.t.}\begin{cases} g_j(\boldsymbol{x}) = E_j \Lambda_j \left(\Lambda_j^2 + 1\right) \le 0,\ j = 1,\ldots,N_e \\ g_{N_e+1}(\boldsymbol{x}) = \Gamma\left(\Gamma^2 + 1\right) \le 0,\ g_{N_e+2}(\boldsymbol{x}) = \Pi\left(\Pi^2 + 1\right) \le 0, \\ g_{N_e+3}(\boldsymbol{x},\boldsymbol{A}) = \Phi\left(\Phi^2 + 1\right) \le 0 \end{cases} \tag{10}$$

with

$$\Lambda_j = \sigma_j^v / \sigma_{\lim} - 1,\ \ \Gamma = \frac{\boldsymbol{m}^T\boldsymbol{I}}{a_r \boldsymbol{m}_{\boldsymbol{fe}}^T \boldsymbol{I}} - 1$$
$$\Pi = \frac{C}{C_0} - 1,\ \Phi = \frac{T_{vr}}{T_{vr0}} - 1 \tag{11}$$

The setting of the reference values is according to the optimization requirements and the motor performance.

D. System Equation of the FEA for Performance Calculation

Excited with symmetrical three-phase current, the magnetostatic field FEA is adopted for the electromagnetic performance calculation in this research. The system equation of the electromagnetic field FEA can be summarized as the solution of

$$\boldsymbol{SA} - \boldsymbol{q} = \boldsymbol{0} \tag{12}$$

where $\boldsymbol{S}$ is the coefficient matrix, $\boldsymbol{A}$ the vector of nodal vector potentials to be solved, and $\boldsymbol{q}$ the excitation source vector. The system matrix of the static mechanical FEA has the same form as

$$\boldsymbol{KU} - \boldsymbol{f} = \boldsymbol{0} \tag{13}$$

where $\boldsymbol{K}$ is the coefficient matrix in the static mechanical system, $\boldsymbol{U}$ the displacement vector computed to be solved, and $\boldsymbol{f}$ the load vector. The coupling effect between the electromagnetic and mechanical fields is not within the scope of this study. In this research, the centripetal force is considered as the load on the rotating rotor, and the load of each element can be calculated by

$$f_e = m_e r_e \omega_e^2 \tag{14}$$

where f_e is the centripetal force of each element, m_e the element mass, r_e the radius of the element, and ω_e the angular velocity.

After the FEA system equations are solved, the motor performances in (8) can be computed. Meanwhile, for solving the topology optimization problem, the system equation information will also be utilized for the sensitivity computation of the design variables. The detailed computation method is introduced in the section below.

III. Topology Optimization Based on the Augmented Lagrangian Method

As illustrated in (8), there are electromagnetic and mechanical constraints in the optimization. Since the stress in the model is an element property, the number of stress constraints equals to the element number in the rotor dimension. Therefore, the total constraint number is extremely high in the optimization model of SynRM, which aggravates the difficulty

of problem-solving. To alleviate the difficulty, the AL method is adopted and introduced in detail below.

A. Establishment of the Augmented Lagrangian Method

Utilizing the normalized AL method, one can transfer the optimization problem with high dimensional constraints into a unconstrainted problem [24] and rewrite the objective function as

$$J\left(\boldsymbol{x},\boldsymbol{A},\boldsymbol{U}\right)=f\left(\boldsymbol{x},\boldsymbol{A}\right)+\frac{1}{N}P(\boldsymbol{x},\boldsymbol{A},\boldsymbol{U}) \tag{15}$$

where $N=N_e+3$, which equals the number of the constraints. The penalization term is expressed as

$$P=\sum_{j=1}^{N}\left[\zeta_j h_j+\frac{\chi}{2}h_j^{\,2}\right] \tag{16}$$

and

$$h_j=\max\left[g_j,-\frac{\zeta_j}{\chi}\right] \tag{17}$$

The coefficient χ and Lagrange multiplier for the iteration step k+1 requires to be updated as

$$\chi^{(k+1)}=\min\left[\alpha\chi^{(k)},\chi_{\max}\right] \tag{18}$$

$$\zeta_j^{(k+1)}=\zeta_j^{(k)}+\chi^{(k)}h_j \tag{19}$$

where $\chi_{\max}$ is the upper limit of χ, and α the gain coefficient. Then AL method is established for the solution of the optimization with high dimensional constraints.

B. Sensitivity Analysis and Topology Optimization Framework Building

Based on the established AL model, the explicit sensitivity should be calculated for applying gradient-based algorithms to solve the high dimensional minimization problem. Following the chain rule, the sensitivity of the AL function to the design variables can be calculated as

$$\frac{\mathrm{d}J}{\mathrm{d}\boldsymbol{x}}=\frac{\partial\boldsymbol{\nu}}{\partial\boldsymbol{x}}\frac{\mathrm{d}J}{\mathrm{d}\boldsymbol{\nu}}+\frac{\partial\boldsymbol{E}}{\partial\boldsymbol{x}}\frac{\mathrm{d}J}{\mathrm{d}\boldsymbol{E}}+\frac{\partial\boldsymbol{m}}{\partial\boldsymbol{x}}\frac{\mathrm{d}J}{\mathrm{d}\boldsymbol{m}} \tag{20}$$

By ignoring the coupling effect between the electromagnetic and mechanical fields, the sensitivity computation (20) can be simplified as

$$\frac{\mathrm{d}J}{\mathrm{d}\boldsymbol{x}}=\frac{\partial\boldsymbol{\nu}}{\partial\boldsymbol{x}}\left(\frac{\partial f}{\partial\boldsymbol{\nu}}+\frac{1}{N}\frac{\partial P}{\partial\boldsymbol{\nu}}\right)+\frac{\partial\boldsymbol{E}}{\partial\boldsymbol{x}}\left(\frac{1}{N}\frac{\partial P}{\partial\boldsymbol{E}}\right)+\frac{1}{N}\frac{\partial\boldsymbol{m}}{\partial\boldsymbol{x}}\left(\frac{\partial P}{\partial\boldsymbol{m}}\right) \tag{21}$$

Accordingly, the sensitivity computation can be divided into the derivation of the material property to the design variables and the derivation of the objective function to the material properties. Taking the reluctivity as an example, one can calculate the partial derivation as

$$\frac{\partial\nu}{\partial x}=\frac{\partial\nu}{\partial f_p}\frac{\partial f_p}{\partial y}\frac{\partial y}{\partial x} \tag{22}$$

According to the chain rule, the derivation of the objective function to the element reluctivity can be unfolded as

$$\frac{\partial f}{\partial\nu_e}=\frac{\partial f}{\partial\boldsymbol{T}^T}\frac{\partial\boldsymbol{T}}{\partial\nu_e} \tag{23}$$

where ν_e is the reluctivity of element e, and $\boldsymbol{T}$ the torque vector calculated in sampled rotor points by Maxwell tensor method. The torque sensitivity at the i_{th} rotor angle can be calculated by the adjoint method as

$$\frac{\mathrm{d}T_i}{\mathrm{d}\nu_{\mathrm{e}}}=\boldsymbol{\lambda}_i^{\,T}\frac{\partial\boldsymbol{S}_i}{\partial\nu_{\mathrm{e}}}\Big|_{\boldsymbol{A}_i=\mathrm{const}}\boldsymbol{A}_i \tag{24}$$

Considering the nonlinearity of the electromagnetic system, one can solve the adjoint vector by

$$\boldsymbol{\lambda}_i^{\,T}\left(\boldsymbol{S}_i+\frac{\partial\boldsymbol{S}_i}{\partial\boldsymbol{A}_i}\boldsymbol{A}_i\right)=-\frac{\partial T_i}{\partial\boldsymbol{A}_i^T} \tag{25}$$

with the computed $\boldsymbol{\lambda}_i$, the sensitivity computation (24) can be completed. Then the derivation of f to the design variable vector $\boldsymbol{x}$ can be obtained. Following the same process as expressed by (22), the derivation of Young's modulus $\boldsymbol{E}$ and mass $\boldsymbol{m}$ to the design variables can also be calculated according to the specific interpolation scheme shown in (6) and (7). Similarly, the penalization function sensitivity to the element material property parameter can be expressed as

$$\frac{\partial P}{\partial E_e}=\sum_{j=1}^{N}\left[\left(\zeta_j+\chi h_j\right)\left(\frac{\partial h_j}{\partial E_e}+\frac{\partial h_j}{\partial\boldsymbol{U}}\cdot\frac{\partial\boldsymbol{U}}{\partial E_e}\right)\right] \tag{26}$$

$$\frac{\partial P}{\partial\nu_e}=\sum_{j=1}^{N}\left[\left(\zeta_j+\chi h_j\right)\left(\frac{\partial h_j}{\partial\nu_e}+\frac{\partial h_j}{\partial\boldsymbol{A}}\cdot\frac{\partial\boldsymbol{A}}{\partial\nu_e}\right)\right] \tag{27}$$

$$\frac{\partial P}{\partial m_e}=\sum_{j=1}^{N}\left[\left(\zeta_j+\chi h_j\right)\left(\frac{\partial h_j}{\partial m_e}+\frac{\partial h_j}{\partial\boldsymbol{U}}\cdot\frac{\partial\boldsymbol{U}}{\partial m_e}\right)\right] \tag{28}$$

Then, we can use the adjoint method to avoid the computation of the partial derivate of the displacement vector or magnetic vector potential to the material property, e.g., $\partial\boldsymbol{U}/\partial E_e$, to accelerate the sensitivity computing. Taking the derivation of the penal function P to element Young's modulus as an example, one can express the formulation as

$$\begin{aligned}\frac{\partial P}{\partial E_e}&=\sum_{j=1}^{N}\left[\left(\zeta_j+\chi h_j\right)\left(\frac{\partial h_j}{\partial E_e}+\frac{\partial h_j}{\partial\boldsymbol{U}}\cdot\frac{\partial\boldsymbol{U}}{\partial E_e}\right)\right]+\boldsymbol{\lambda}_E^T\frac{\partial(\boldsymbol{K}\boldsymbol{U}-\boldsymbol{f})}{\partial E_e}\\&=\sum_{j=1}^{N}\left[\left(\zeta_j+\chi h_j\right)\left(\frac{\partial h_j}{\partial E_e}+\frac{\partial h_j}{\partial\boldsymbol{U}}\cdot\frac{\partial\boldsymbol{U}}{\partial E_e}\right)\right]\\&\quad+\boldsymbol{\lambda}_E^T\left(\frac{\partial\boldsymbol{K}}{\partial E_e}\boldsymbol{U}+\boldsymbol{K}\frac{\partial\boldsymbol{U}}{\partial E_e}-\frac{\partial\boldsymbol{f}}{\partial E_e}\right)\\&=\sum_{j=1}^{N}\left(\zeta_j+\chi h_j\right)\frac{\partial h_j}{\partial E_e}+\boldsymbol{\lambda}_E^T\frac{\partial\boldsymbol{K}}{\partial E_e}\boldsymbol{U}-\boldsymbol{\lambda}_E^T\frac{\partial\boldsymbol{f}}{\partial E_e}\\&\quad+\left[\sum_{j=1}^{N}\left(\zeta_j+\chi h_j\right)\frac{\partial h_j}{\partial\boldsymbol{U}}+\boldsymbol{\lambda}_E^T\boldsymbol{K}\right]\frac{\partial\boldsymbol{U}}{\partial E_e}\end{aligned} \tag{29}$$

Let

$$\sum_{j=1}^{N}\left(\zeta_j+\chi h_j\right)\frac{\partial h_j}{\partial\boldsymbol{U}}+\boldsymbol{\lambda}_E^T\boldsymbol{K}=0 \tag{30}$$

The adjoint vector can be obtained by solving (30). With the achieved $\boldsymbol{\lambda}_E^T$, (29) can be calculated by

$$\frac{\partial P}{\partial E_e}=\sum_{j=1}^{N}\left(\zeta_j+\chi h_j\right)\frac{\partial h_j}{\partial E_e}+\boldsymbol{\lambda}_E^T\frac{\partial\boldsymbol{K}}{\partial E_e}\boldsymbol{U}-\boldsymbol{\lambda}_E^T\frac{\partial\boldsymbol{f}}{\partial E_e} \tag{31}$$

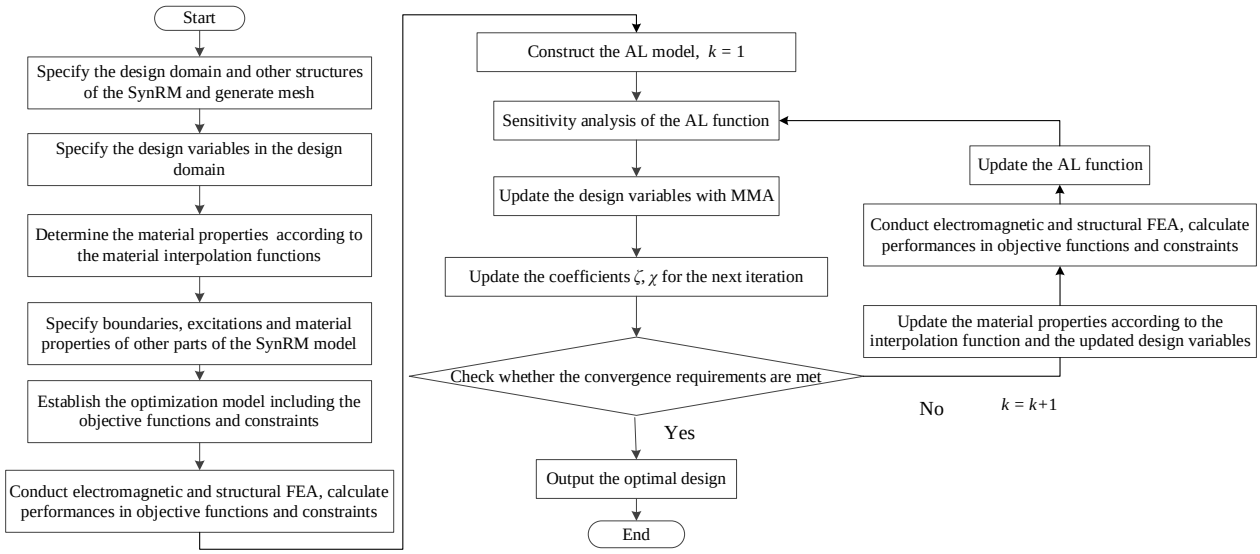

Fig. 5. Flowchart of the developed topology optimization method for rotor design of SynRMs.

By the same derivation process above, (27) and (28) can be written as

$$\frac{\partial P}{\partial \nu_e}=\sum_{j=1}^{N}\left(\zeta_j+\chi h_j\right)\frac{\partial h_j}{\partial \nu_e}+\boldsymbol{\lambda}_v^T\frac{\partial \boldsymbol{S}}{\partial \nu_e}\boldsymbol{A}-\boldsymbol{\lambda}_v^T\frac{\partial \boldsymbol{q}}{\partial \nu_e} \tag{32}$$

$$\frac{\partial P}{\partial m_e}=\sum_{j=1}^{N}\left(\zeta_j+\chi h_j\right)\frac{\partial h_j}{\partial m_e}+\boldsymbol{\lambda}_m^T\frac{\partial \boldsymbol{K}}{\partial m_e}\boldsymbol{U}-\boldsymbol{\lambda}_m^T\frac{\partial \boldsymbol{f}}{\partial m_e} \tag{33}$$

where the adjoint vectors in (32) and (33) can be obtained by following the same step as (30). Then the derivation of P to the design variable vector $\boldsymbol{x}$ can be completed.

With the obtained sensitivities of the AL function, the minimization then can be solved by gradient-based algorithms. In this research, the method of moving asymptotes (MMA) is adopted to minimize the AL function. Based on the AL method, Fig. 5 illustrates the complete optimization framework developed in this research. The left column of the flowchart describes the basic setting steps for the optimization which includes the FEA modeling, material interpolation and optimization domain, and objectives and constraints should be established. Then, the AL function can be constructed for decreasing the computation difficulty caused by the high number of constraints. The sensitivity analysis of the design variables to the established AL model is then conducted for the minimization problem solving with an optimization algorithm. Taking advantage of MMA and the coefficient updated scheme, the optimization problem is solved by iteration until the convergence requirements are met.

IV. Result Comparison and Discussion

A. A 3 kW SynRM Design Example

Topology optimization of the SynRM example shown in Fig .2 is performed. The element number in the design domain, i.e. the design variable number is 1879. The specific dimension, electrical and material parameters are listed in Table I. Specifically, the torque of SynRM with the initial guess rotor structure is 1.78 N·m.

TABLE I
Specifications of the Motor and Rotor Material

Parameters	Unit	Value
Stator outer diameter	mm	155
Stator inner diameter	mm	90
Rotor inner diameter	mm	28
Air gap	mm	0.5
Axial length	mm	100
Number of phases		3
Number of poles		4
Number of teeth		24
Rated speed	rpm	2500
Advanced angle	Electrical Degree	45
Phase current amplitude	A	26
Torque of the initial guess structure	N·m	1.78
Electrical steel		B35A300
Young's module	Mpa	2×10^5

The specific design objective is defined to maximize average torque at 2500 rpm. For the electromagnetic torque profile computation, 30 rotor positions are sampled evenly in 60 electrical degrees. Regarding the mechanical analysis, the same mesh of the electromagnetic model is adopted while the load is the centripetal force for the rotating structure. The inner structural boundary connected to the shaft is fixed which is conducted by setting the displacement of the nodes as 0. To guarantee structural reliability, the maximum stress and structural compliance of the structure should be limited. Specifically, the stress and structural compliance are computed at speed of 10000 rpm to guarantee the strength of the rotor at high-speed operation.

TABLE II
Parameter Setting for the Optimization Model

Performance	Unit	Value
C_0		5×10^{-3}
T_{vr0}	$(\mathrm{N\cdot m})^2$	0.2
a_r		1
σ_{lim}	Mpa	200

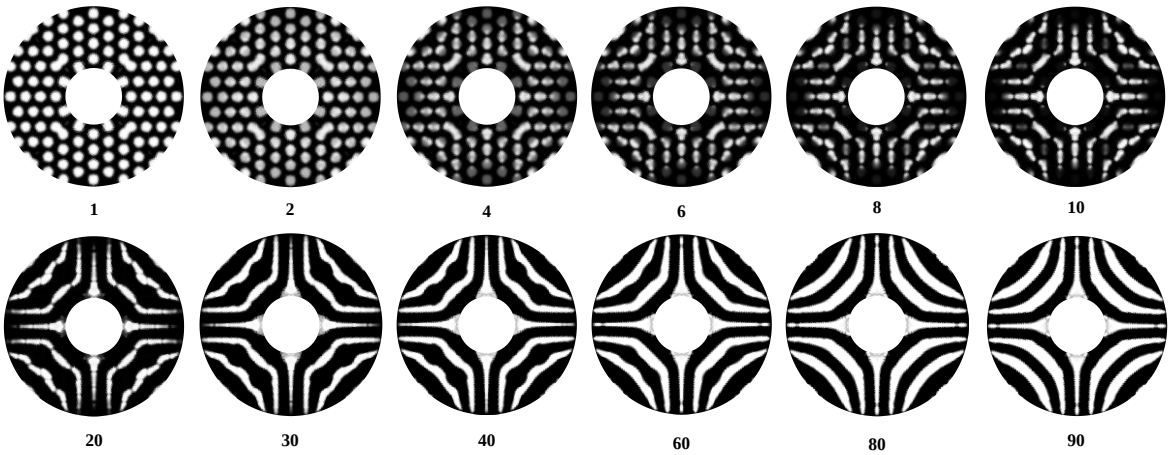

Fig. 6. Topology variation of different steps in the optimization iteration process.

Table II lists the limited electromagnetic or structural parameters in the optimization model. Since the working condition and dimensions etc. of different machines may differ from each other, the selection of the C_0, T_{vr0}, and a_r generally depends on the design requirements. The selection of the C_0 depends on the dimension, rotating speed, and material property etc. The value setting can refer to the compliance of the initial guess structure etc. a_r is the ratio of the electrical steel in the design domain, it is generally set less than 1. When there is a specific constraint of the electrical steel using quantity, a_r can be set according to the requested material using quantity. T_{vr0} is the torque ripple reference value, which is expected as a small value. It is chosen can refer to the torque ripple values of the existing designs. Moreover, the above 3 parameters can also be adjusted adaptively in the optimization iteration for obtaining a high-performance design.

B. Optimization Results and Analysis

The topology optimization is performed on a ASUS TUF Gaming F17 laptop, with Intel(R) Core(TM) i7-12700H 2.3 GHz processer, 14 physical cores, and 16 GB RAM. The optimization with 90 iterations is finished in 1.3 hours.

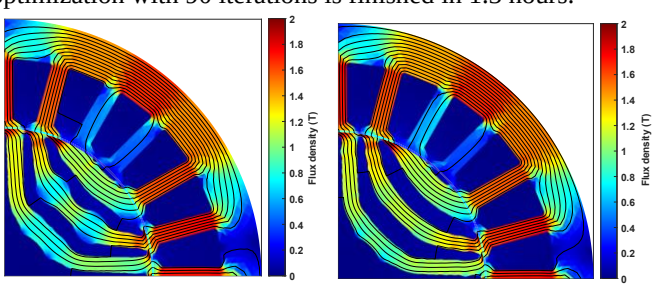

(a) (b)

Fig. 7. Flux density and flux line distribution at (a) 40_{th} step and (b) 80_{th} step.

The $f_p(\boldsymbol{y})$ value in (4) is mapped into Fig. 6 to demonstrate the topology variation of the rotor structure in the topology optimization process. The geometry of the structure evolves from a multi-hole structure to one with multi-layer magnetic barriers. The basic conceptual structure is generated after the front 10 steps. In the following steps, the clear boundary between the electrical steel and air is progressively generated, and the virtual material with the intermediate material property can be eliminated effectively. The redundant structure, such as the bulge in the middle steel barrier in the front steps is removed. Fig. 7 illustrates the flux density distribution comparison between the designs of the 40_{th} and 80_{th} steps (before and after the redundant structure is deleted), respectively.

Fig. 8 shows the torque profile improvement in the optimization process. The average torque increases rapidly in the first 50 iteration steps and reaches relatively stable in the following steps. On the other hand, after the immediate rising at the beginning of the optimization, the torque ripple is reduced effectively in the following iteration.

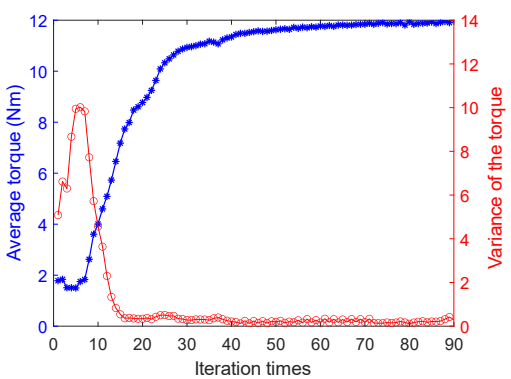

Fig. 8. Torque profile improvement with respect to iteration steps.

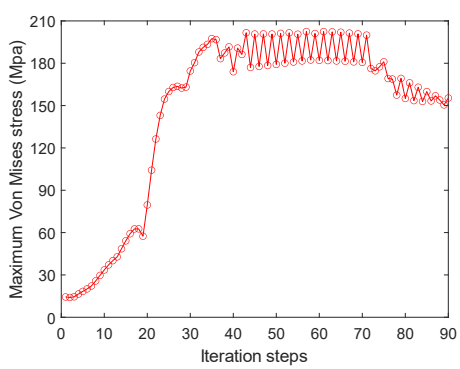

Fig. 9. Maximum Von Mises stress variation with respect to iteration steps.

Fig. 9 demonstrates the variation of the maximum Von Mises stress in the iteration process. Fig. 10 presents the Von Mises stress distribution of the 61_{st} and 80_{th} rotor structures in

the iteration. The concentration point of the stress happens on the thin rib close to the air gap. There is the part in the 61_{st} design that exceeds the stress limit. By the developed AL function with coefficient updating scheme, the maximum stress of the rotor is well limited below the set permissible yield stress value after limited steps of iteration. As shown in Fig. 10, the maximum stress of the 80_{th} rotor structure is lower than the limited stress.

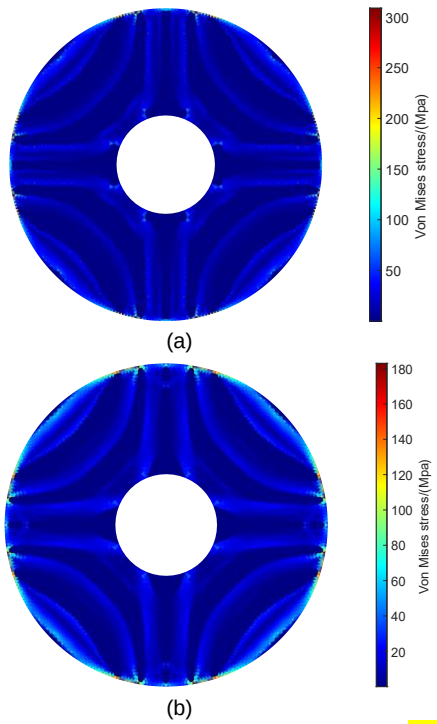

Fig. 10 Von Mises stress distribution of the rotor at (a) 61_{st} step and (b) 80_{th} step.

By considering the performance comprehensively, the design result of the 80_{th} step is selected as the optimal solution. The average output torque of the optimized design is 11.9 N·m, the output power is 3.1 kW at the rated speed, and the torque ripple (defined by the variance of the torque at the computed rotor angles) is 0.14 $(N \cdot m)^2$. The maximum Von Mises of the structure is 155 Mpa, and the structural compliance of the optimized design is 4.5×10^{-3} N·m. Fig. 11 shows the torque profile of the obtained structure.

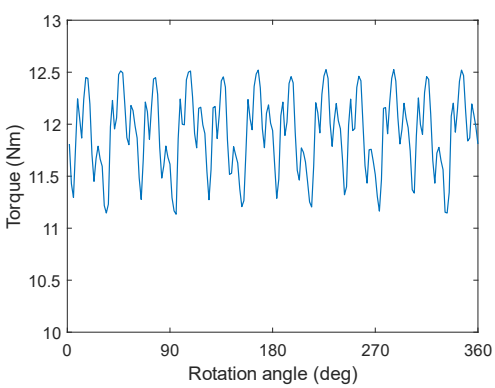

Fig. 11. Torque profile of the obtained design.

Furthermore, to verify the output performance of the rotor design obtained by the topology optimization method. We take advantage of a parametric design optimization method for optimizing the rotor topology in a parameter optimization approach. By applying the parameter optimization developed in [25], the design optimization problem of the SynRM with around 10 shape methods is transferred into a 3 parameter design optimization problem. The obtained optimized structure is shown in Fig. 12. The torque profile comparison of the optimized designs is compared in Table III. It can be observed that the optimization result obtained by the topology optimization shows a slightly higher average torque and better torque variance performance. In terms of the computational burden, FEA of samples produced in the optimization process accounts for the main computation cost. 180 samples are generated for the FEA computation in the parameter optimization process, while 90 samples are generated in the topology optimization. The comparison results proved the effectiveness of the proposed topology optimization method.

TABLE III
PERFORMANCE COMPARISON OF THE OPTIMIZED STRUCTURES

Performance	Unit	Parameter optimization	Topology optimization
Average torque	N·m	11.42	11.92
Torque variance	$(N \cdot m)^2$	0.54	0.14
Saliency ratio		4.95	5.4

Fig. 12 optimized structure by the parameter optimization method [25]

C. Discussion on the Influence Factors on the Topology Optimization Based on a 15 kW SynRM Design Example

TABLE IV
SPECIFICATIONS OF THE 15 KW MOTOR AND ROTOR MATERIAL

Parameters	Unit	Value
Stator outer diameter	mm	205
Stator inner diameter	mm	124
Rotor inner diameter	mm	28
Air gap	mm	1
Axial length	mm	150
Number of phases		3
Number of poles		4
Number of teeth		36
Rated speed	rpm	3000
Phase current amplitude	A	50
Electrical steel		M350-50A
Young's module	Mpa	2×10^5

Considering the features of the high dimension, high nonlinearity and multiple peak value etc. of the motor topology optimization, the final optimized structure can be easily affected by the optimization modeling, working condition, and the structure dimension parameters. On the other hand, due to

the application of the gradient-based optimization algorithm for decreasing the optimization difficulty and accelerating the solving speed, the optimized geometry can also be influenced by the initial guess structure. considering the above-mentioned factors, the influence of initial design and current angle on the optimized structures is investigated through a 15 kW case study. The basic parameters of the motor are presented in Table IV. Table V lists the reference values in the optimization model.

TABLE V

PARAMETER SETTING FOR THE OPTIMIZATION MODEL

Performance	Unit	Value
C_0		0.03
T_{vr0}	$(N \cdot m)^2$	15
σ_{lim}	Mpa	305

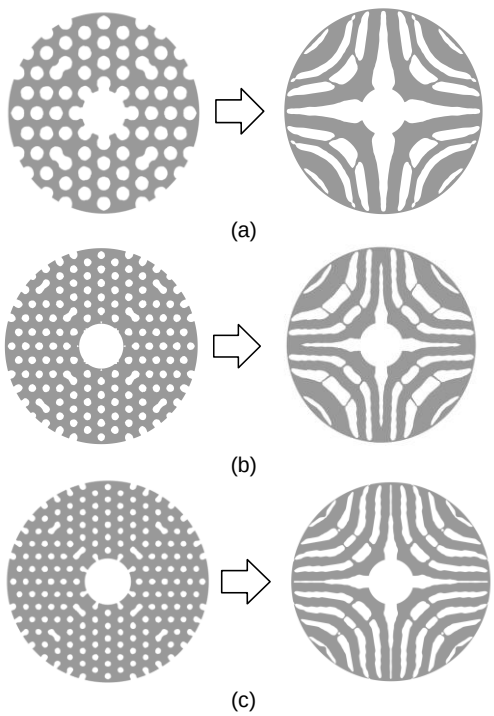

Fig. 13 Initial guess structure influence on the optimized structure

TABLE VI

PERFORMANCES OF THE OPTIMIZED STRUCTURES

Performance	Unit	Design (a)	Design (b)	Design (c)
C		0.0289	0.0138	0.0108
T_{vr}	$(N \cdot m)^2$	12.89	10.66	9.02
Maximum stress	Mpa	294.47	150.15	144.32
Average Torque	$N \cdot m$	53.59	56.11	54.01

To investigate the influence of the initial design, topology optimization is performed starting from structures with different hole numbers and distributions. Fig. 13 illustrates the initial guess structure and the relevant optimized design. It can be observed that both the flux barrier layer number and the shape of the structure can be affected by the initial number. Table VI lists the performance difference caused by the different rotor structures. The mechanical FEA is conducted at the speed of 10000 rpm. It is worth noting that ribs are generated in the topology optimization condition of the 15 kW design example. The reasons of the rib generation may include operation conditions, the larger rotor diameter compared with the 3 kW case, and the mechanical constraints about the structural compliance and stress in the optimization model, etc.

To investigate the influence of the current angle, the SynRM models with the current angle between 45° and 65° are sampled under the same initial guess structure as shown in Fig. 13 (b) and optimized with the proposed method. Fig. 14 demonstrates the rotor structure together with the stator geometry. It can be observed that the optimized topology varies from each other. The optimized structure under the 54° current angle has the best average output 62.2 $N \cdot m$ and its torque variance value is 6.96 $(N \cdot m)^2$. The design under the 51° current angle has the lowest torque variance 4.18 $(N \cdot m)^2$ and its average torque is 57 $N \cdot m$.

Therefore, for compensating the impact of the start design on the optimal design, multiple initial designs can be attempted. On the other hand, if there is a requirement for considering the current angle influence on the optimized structure, such as the design optimization for the maximum torque per ampere operation, the design optimization under the different current angles (especially angles in 50°-55°) can be conducted.

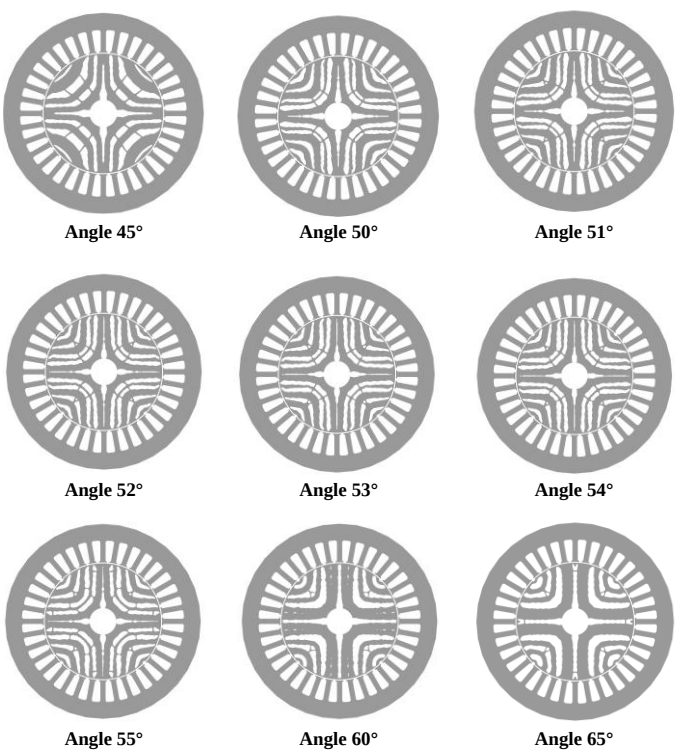

Fig. 14 optimized rotor structure under different current angles.

V. PROTOTYPING AND EXPERIMENT VERIFICATION

The obtained rotor design of the 3 kW design example by the topology optimization is manufactured for experimental verification. Fig. 15 illustrates the rotor prototype with the support structure and the stator within the iron casing. For the manufacturing of the support structure inner the rotor, the stainless steel of low permeability is selected for preventing the flux leakage between the adjacent electrical steel flux carriers.

The experiment rig setup for the performance testing of the SynRM prototype is demonstrated in Fig. 16. To verify the output performance of the prototype, the field-oriented control

is applied with the Rtunit control studio, and the control diagram is presented in Fig. 17. The experiment is conducted under the rated current, i.e., the amplitude value of the phase current is 26 A, and the advanced angle is 45°. Fig. 18 demonstrates the measured output torque and the currents. The measured average torque is 11.3 N · m, which is in good agreement with the computed 11.9 N · m of the optimized design. The 5% error may come from the difference in the material property, the error between the FEA and experiment, and mechanical loss such as the friction loss of the bearings, etc.

(a) (b)

Fig. 15 Manufactured (a) rotor with the support structure and (b) stator.

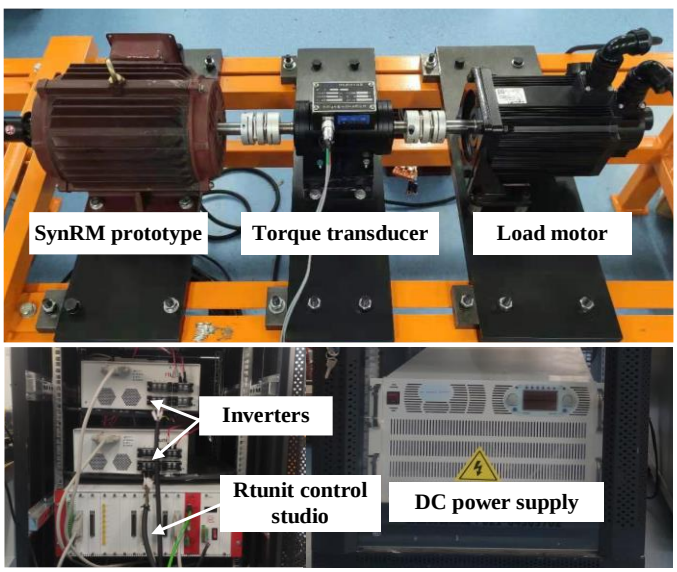

Fig. 16. Experiment rig of the SynRM prototype.

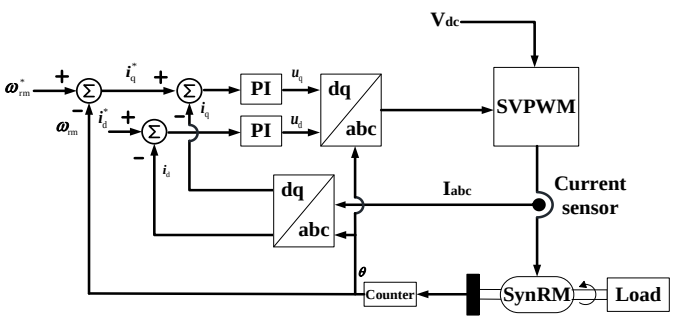

Fig. 17. Control diagram for the SynRM output performance test.

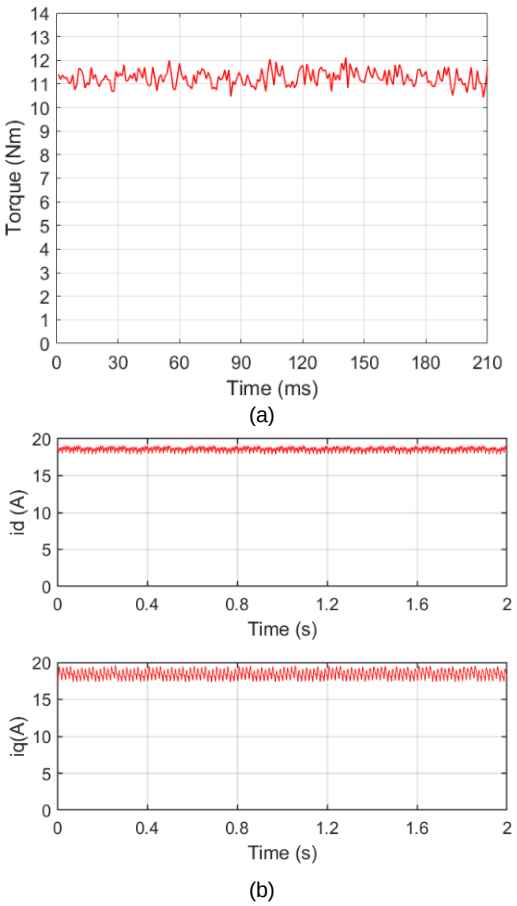

Fig. 18. Measured (a) torque and (b) current of the SynRM prototype.

The torque profile is tested under the low speed of 30 rpm with the rated current and the sampling step is 20 ms. The measured torque profile is shown in Fig. 19. The tested torque variance value is 0.245 $(N \cdot m)^2$ which is higher than the computed value of 0.14 $(N \cdot m)^2$. The accurate test of the torque ripple is regarded as a challenge in the research field. The error may come from various sources, e.g. the load current cannot be promised ideally sinusoidal. Since the 0.14 $(N \cdot m)^2$ is computed by the FEA model which is regarded as of high accuracy for the computation motor performance, the optimization can be regarded as a success. It can be also observed that the torque ripple is relatively small, which proves the effectiveness of optimization.

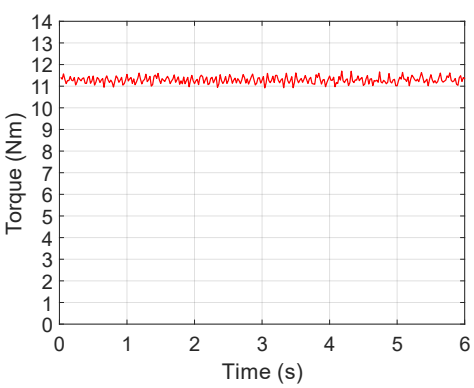

Fig. 19. Measured torque profile at low speed.

The maximum speed 10000 rpm has been tested in the light load condition. It was also tried to be dragged to the speed by the high-speed traction machine. The rotor integrity is well ensured.

VI. Conclusion

This research proposes a multi-physics topology optimization method for high freedom and automatic design of SynRM rotors considering the electromagnetic and mechanical performances, including the output torque, mechanical stiffness, strength, and weight of the rotor. An AL framework has been established for solving optimization problems with high dimensional constraints (mainly caused by the stress constraints). A prototype of the optimized SynRM rotor structure has been manufactured and tested. The experimental results validate the effectiveness of the optimized design. The proposed topology optimization framework can be an effective approach for automatic conceptual and quantitative structural optimization of other types of electrical machines with high dimensional constraints.

VII. References

[1] M. Bugsch and B. Piepenbreier, "High-bandwidth sensorless control of synchronous reluctance machines in the low- and zero-Speed Range," *IEEE Trans. Ind. Appl.*, vol. 56, no. 3, pp. 2663-2672, 2020, doi: 10.1109/TIA.2020.2969123.

[2] T. Kojima, T. Suzuki, M. Hazeyama, and S. Kayano, "Position sensorless control of synchronous reluctance machines based on magnetic saturation depending on current phase angles," *IEEE Trans. Ind. Appl.*, vol. 56, no. 3, pp. 2171-2179, 2020, doi: 10.1109/TIA.2020.2970828.4.

[3] Y. Hu, B. Chen, Y. Xiao, J. Shi, and L. Li, "Study on the influence of design and optimization of rotor bars on parameters of a line-start synchronous reluctance motor," *IEEE Trans. Ind. Appl.*, vol. 56, no. 2, pp. 1368-1376, 2020, doi: 10.1109/TIA.2019.2962431.

[4] Y. Wang and N. Bianchi, "Performance analysis of self-excited reluctance generating system using power balance," in IEEE Transactions on Energy Conversion, vol. 34, no. 2, pp. 673-679, June 2019, doi: 10.1109/TEC.2018.2880835.

[5] M. D. Nardo, G. L. Calzo, M. Galea and C. Gerada, "Design optimization of a High-Speed Synchronous Reluctance Machine," *IEEE Trans. Ind. Appl*, vol. 54, no. 1, pp. 233-243, Jan.-Feb. 2018.doi: 10.1109/TIA.2017.2758759

[6] C. Babetto, G. Bacco and N. Bianchi, "Synchronous reluctance machine optimization for high-speed applications," in IEEE Transactions on Energy Conversion, vol. 33, no. 3, pp. 1266-1273, Sept. 2018. doi: 10.1109/TEC.2018.2800536

[7] C. Liu, K. Wang, S. Wang, Y. Wang and J. Zhu, "Torque ripple reduction of synchronous reluctance machine by using asymmetrical barriers and hybrid magnetic core," *CES Transactions on Electrical Machines and Systems*, vol. 5, no. 1, pp. 13-20, March 2021.

[8] M. P. Bendsøe and N. Kikuchi, "Generating optimal topologies in structural design using a homogenization method," *Comput. Methods Appl. Mech. Eng.* , vol. 71, no. 2, 197-224, Nov. 1988.

[9] O. Sigmund and K. Maute, "Topology optimization approaches," *Struct. Multidisciplinary Optim.*, vol. 48, no. 6, pp. 1031-1055, Dec. 2013.

[10] H. Zhang, W. Xu, S. Wang, Y. Huangfu, G. Wang, and J. Zhu, "Optimum design of rotor for high-speed switched reluctance motor using level set method," *IEEE Trans. Magn*., vol. 50, no. 2, pp. 765-768, 2014.

[11] G. Bramerdorfer, J. A. Tapia, J. J. Pyrhönen, and A. Cavagnino, "Modern electrical machine design optimization: techniques, trends, and best practices," *IEEE Trans. Ind. Electron.*, vol. 65, no. 10, pp. 7672-7684, Oct. 2018.

[12] B. Ma, J. Zheng, G. Lei, J. Zhu, P. Jin and Y. Guo, "Topology optimization of ferromagnetic components in electrical machines," *IEEE Transactions on Energy Conversion*, vol. 35, no. 2, pp. 786-798, June 2020, doi: 10.1109/TEC.2019.2960519.

[13] Y. Yamashita and Y. Okamoto, "Design optimization of synchronous reluctance motor for reducing iron loss and improving torque characteristics using topology optimization based on the level-set method," *IEEE Trans. Magn*., vol. 56, no. 3, pp. 1-4, March 2020, Art no. 7510704.

[14] E. Kuci, M. Jansen, and O. Coulaud, "Level set topology optimization of synchronous reluctance machines using a body-fitted mesh representation," *Structural and Multidisciplinary Optimization*, vol. 64, no. 6, pp. 3729-3745, 2021/12/01 2021, doi: 10.1007/s00158-021-03049-0.

[15] Y. Otomo and H. Igarashi, "Topology optimization using Gabor filter: application to synchronous reluctance motor," *IEEE Trans. Magn*., pp. 1-1, 2021, doi: 10.1109/tmag.2021.3057402.

[16] S. Barmada, N. Fontana, L. Sani, D. Thomopulos, and M. Tucci, "Deep learning and reduced models for fast optimization in electromagnetics," *IEEE Trans. Magn*., vol. 56, no. 3, pp. 1-4, 2020, doi: 10.1109/tmag.2019.2957197.

[17] A. Credo, G. Fabri, M. Villani, and M. Popescu, "Adopting the topology optimization in the design of high-speed synchronous reluctance motors for electric vehicles," *IEEE Trans. Ind. Appl.*, vol. 56, no. 5, pp. 5429-5438, 2020.

[18] A. Credo, G. Fabri, M. Villani and M. Popescu, "High speed Synchronous reluctance motors for electric vehicles: a focus on rotor mechanical design,"*2019 IEEE International Electric Machines & Drives Conference (IEMDC)*, San Diego, CA, USA, 2019, pp. 165-171.doi: 10.1109/IEMDC.2019.8785083

[19] C. Lee, J. Lee and I. G. Jang, "Topology optimization for the manufacturable and structurally safe synchronous reluctance motors with multiple iron webs and bridges," *IEEE Trans. Ind. Electron.*,early access doi: 10.1109/TIE.2022.3148751

[20] O. Korman, M. Di Nardo, M. Degano and C. Gerada, "On the use of topology optimization for synchronous reluctance machines design", *Energies*, vol.15, pp. 3719, May 2022, doi: 10.3390/en15103719.

[21] O. Korman, M. Di Nardo, M. Degano and C. Gerada, "On the use of topology optimization for synchronous reluctance machines design", *Energies*, vol.15, pp. 3719, May 2022, doi: 10.3390/en15103719.

[22] F. Guo and I. P. Brown, "Simultaneous magnetic and structural topology optimization of synchronous reluctance machine rotors," *IEEE Trans. Magn*., vol. 56, no. 10, pp. 1-12, 2020, doi: 10.1109/TMAG.2020.3014289.

[23] C. S. Andreasen, M. O. Elingaard, and N. Aage, "Level set topology and shape optimization by density methods using cut elements with length scale control," *Struct. Multidisciplinary Optim.*, vol. 62, no. 2, pp. 685-707, 2020/08/01 2020, doi: 10.1007/s00158-020-02527-1.

[24] O. Giraldo-Londoño and G. H. Paulino, "PolyStress: a Matlab implementation for local stress-constrained topology optimization using the augmented Lagrangian method," *Struct. Multidisciplinary Optim.*, vol. 63, no. 4, pp. 2065-2097, 2021/04/01 2021, doi: 10.1007/s00158-020-02760-8.

[25] R. -R. Moghaddam and F. Gyllensten, "Novel high-performance SynRM design method: An easy approach for a complicated rotor topology," *IEEE Trans. Ind. Electron.*, vol. 61, no. 9, pp. 5058-5065, Sept. 2014, doi: 10.1109/TIE.2013.2271601.

Yu Li received the M.S degree in Mechanical Engineering form Hunan University of Science and Technology, Hunan, China, in 2017. He is currently working toward the Ph.D. degree in electrical engineering with the College of Electrical and Information Engineering, Hunan University, Changsha, China.

His expertise covers multi-physics simulation and topology optimization algorithm. His research interest is the multi-physics topology optimization of electrical machine.

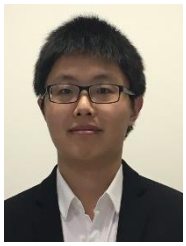

Bo Ma received the B.E. degree from Hefei University of Technology in 2014, and Ph.D. degree from University of Technology Sydney in 2020, all in electrical engineering. Currently, he serves as an assistant professor with the College of Electrical and Information Engineering, Hunan University, Changsha, China.
His current research interests include design optimization of electrical machines and drive systems.

Jing Zheng received the B.E. degree from Hunan University, Changsha, China, in 2012, and Ph.D. degree from University of Technology Sydney (UTS), in 2019, all in mechanical engineering.
She is currently an assistant professor with the School of Mechanical and Vehicle Engineering, Hunan University. Her research interests include structural reliability analysis and topology optimization.

Jianguo Zhu (S'93–M'96–SM'03) received the B.E. degree from Jiangsu Institute of Technology, Zhenjiang, China, in 1982, the M.E. degree from Shanghai University of Technology, Shanghai, China, in 1987, and the Ph.D. degree from the University of Technology Sydney (UTS), Sydney, NSW, Australia, in 1995, all in electrical engineering.
He was appointed as a Lecturer at UTS in 1994 and promoted to Full Professor in 2004 and Distinguished Professor of Electrical Engineering in 2017. At UTS, he has held various leadership positions, including the Head of School for School of Electrical, Mechanical, and Mechatronic Systems and Director for Center of Electrical Machines and Power Electronics. In 2018, he joined the University of Sydney, Sydney, NSW, Australia, as a Full Professor and Head of School for School of Electrical and Information Engineering. His research interests include computational electromagnetics, measurement and modeling of magnetic properties of materials, electrical machines and drives, power electronics, renewable energy systems, and smart microgrids

Gang Lei (M'4) received the B.S. degree in mathematics from Huanggang Normal University, China, in 2003, the M.S. degree in mathematics and Ph.D. degree in electrical engineering from Huazhong University of Science and Technology, China, in 2006 and 2009, respectively.
He is currently a Senior Lecturer with the School of Electrical and Data Engineering, University of Technology Sydney, Sydney, NSW, Australia. His research interests include design optimization and control of electrical drive systems and renewable energy systems.